Anionic and Cationic Redox Processes in β-Li 2 IrO 3 and Their Structural Implications on Electrochemical Cycling in a Li-Ion Cell

Paul Pearce, Gaurav Assat, Antonella Iadecola, François Fauth, Rémi Dedryvère, Artem Abakumov, Gwenaëlle Rousse, Jean-marie Tarascon

Anionic and Cationic Redox Processes in β-Li_2IrO_3 and Their Structural Implications on Electrochemical Cycling in a Li-Ion Cell

Paul E. Pearce[1,2,3,‡], Gaurav Assat[1,2,3,‡], Antonella Iadecola[2], François Fauth[4], Rémi Dedryvère[2,5], Artem Abakumov,[6] Gwenaëlle Rousse[1,2,3] and Jean-Marie Tarascon[1,2,3]*

[1]Collège de France, Chimie du Solide et de l'Energie, UMR 8260, 11 Place Marcelin Berthelot, 75231 Paris Cedex 05, France.
[2]Réseau sur le Stockage Electrochimique de l'Energie (RS2E), FR CNRS 3459, 80039 Amiens Cedex, France.
[3]Sorbonne Université, 4 Place Jussieu, F-75005 Paris, France.
[4]CELLS - ALBA synchrotron, Cerdanyola del Valles, Barcelona E-08290, Spain
[5]IPREM, CNRS, Université de Pau & Pays Adour, E2S-UPPA, Hélioparc, 2 Avenue P. Angot, 64053 Pau Cedex 9, France
[6]Skoltech Center for Energy Science and Technology, Skolkovo Institute of Science and Technology, Moscow 121205, Russian Federation

* Corresponding author: jean-marie.tarascon@college-de-france.fr

‡ P.E.P. and G.A. have contributed equally to this work.

Abstract:

The recent discovery of anionic redox as a means to increase the energy density of transition-metal oxide positive electrodes is now a wellestablished approach in the Li-ion battery field. However, the science behind this new phenomenon pertaining to various Li-rich materials is still debated. Thus, it is of paramount importance to develop a robust set of analytical techniques to address this issue. Herein, we use a suite of synchrotron-based X-ray spectroscopies as well as diffraction techniques to thoroughly characterize the different redox processes taking place in a model Li-rich compound, the tridimensional hyperhoneycomb β-Li_2IrO_3. We clearly establish that the reversible removal of Li^+ from this compound is associated with a previously described reductive coupling mechanism and the formation of the M-(O−O) and M-(O−O)* states. We further show that the respective contributions to these states determine the spectroscopic response for both Ir L_3-edge X-ray absorption spectroscopy and X-ray photoemission spectroscopy. Although the high covalency and the robust tridimensional structure of this compound enable a

high degree of reversible delithiation, we found that pushing the limits of this charge compensation mechanism has significant effects on the local as well as average structure, leading to electrochemical instability over cycling and voltage decay. Overall, this work highlights the practical limits to which anionic redox can be exploited and sheds some light on the nature of the oxidized species formed in certain lithium-rich compounds.

Introduction

As the importance of developing efficient energy storage technologies for transportation and portable electronics continues to increase, so is the motivation to develop high energy density Li-ion batteries. There are two paths to achieving this goal. The first one is by feats of cell engineering, namely, decreasing the amount of dead space and weight. The second is to develop new chemistries, which would enable higher energy density electrodes. Our interest is in the latter and more specifically with a recent paradigm, which is the now well-known anionic redox chemistry.[1-3] Indeed, in the last few years, evidence of the participation of lattice oxygen in certain cathode materials during Li de/insertion has been provided on multiple examples of ordered materials ranging from model ones, such as $Li_2Ru_{1-y}M_yO_3$ (with M = Mn, Sn, Ti) [2-4] and the α and β polymorphs of Li_2IrO_3, [5-7] to more practically-relevant materials such as $Li_{1.2}Ni_{0.13}Mn_{0.54}Co_{0.13}O_2$ (Li-rich NMC). [8-12] Thanks to anionic redox, these materials are capable of attaining specific capacities up to 300 mA.h/g. However, they commonly suffer from voltage decay and capacity loss over cycling in addition to sluggish kinetics and poor energy efficiency due to voltage hysteresis.[8,13-17] These issues make their use in applications challenging.

The performance decay over cycling of Li-rich cathodes has been generally thought to arise from structural instabilities that may accompany the oxidation of lattice oxygen. Indeed, when such materials are pushed to high potentials, their voltage profile gets modified from a staircase profile on first charge to become a sloped one on subsequent cycling, as is the case for all 3d and 4d transition-metal-based Li-rich layered materials.[2-4,7,10,11,13,14] If cycled repeatedly to high potentials, the voltage fades faster, as reported for Li-rich NMC and $Li_2Ru_{0.75}Sn_{0.25}O_3$.[13,18] Similarly, the cycling of Li-rich disordered rock-salt compounds showing anionic redox is also not

very stable.[19] Among the various aforementioned issues, we have previously shown how the tridimensional nature of β-Li_2IrO_3 (Figure 1a) helps in significantly mitigating poor kinetics and voltage hysteresis.6 However, this material still suffers from performance degradation upon cycling, especially when cycled above 4 V vs Li^+/Li. To enable a better understanding of the fundamental origin of such cyclability issues, it is imperative to first clearly characterize the electronic and structural implications of the anionic redox process. This is not a trivial task, as the battery community has come to realize in recent years. Indeed, there is much debate over the validity and relevance of certain characterization techniques used in the past to prove anionic redox activity as well as the ensuing structural changes.[7] While structural changes have been investigated in these materials using an array of state-of-the-art techniques, current understanding remains poor because it is often difficult to probe accurately the local (atomic scale) structural implications of anionic redox in these compounds because we are approaching the limit of characterization techniques. This had led to ongoing debates concerning O−O distance shortening, octahedral distortion, and cation migration.[5,12,20] Similarly, there have been debates surrounding the electronic state of oxygen and the role of metal-oxygen hybridization. As an example, early X-ray photoemission spectroscopy measurements, although successful in providing the first direct evidence of oxygen redox via O 1s spectra, were criticized because usual XPS is a surface-sensitive technique.[21] To increase the XPS probe depth, it was essential to increase the incident X-ray photon energy by using hard X-ray photoemission spectroscopy (HAXPES) using synchrotron radiation. This has enabled us to show unambiguously that the oxidized oxygen observed in XPS spectra is not just a surface phenomenon but is indeed due to a bulk electrochemical process.[22] Likewise, the controversies surrounding early O K-edge X-ray absorption spectroscopy (XAS) [11] were resolved with the recent development of resonant inelastic X-ray scattering (RIXS). [23]

Another challenge in characterizing anionic redox is that it often takes place at high potential, which makes the charged materials highly sensitive not just to moisture in the air but also to the high photon flux provided in synchrotron conditions, especially in some operando experiments needing particularly high brilliance. Ex situ measurements, although subject to other problems (namely, risks of unrepeatability because a different sample is used for each state-of-charge, requiring careful sample preparation, and impossibility to characterize dynamic processes because the samples are relaxed), are more reliable for sensitive samples. Therefore, complementary ex situ and operando characterization techniques must be used to consolidate the findings. With this aim, we used several synchrotron X-ray techniques on the β-Li_2IrO_3 material, which can be completely delithiated and for which anionic redox has been observed on both low and high potential processes.[6] We first revisit the redox processes by complementing Ir L_{III}-edge XAS with Ir 4f and O 1s HAXPES to draw the full picture of the charge compensation mechanism. Then, we use synchrotron X-ray diffraction (XRD) to obtain information on the different phase transitions during the electrochemical delithiation, complemented by neutron powder diffraction (NPD) to obtain information on the positions of oxygen atoms in the cell. Finally, we use the extended X-ray absorption fine structure (EXAFS) to probe the local environment of Ir and examine the distortions of the IrO_6 octahedra to consolidate the results from bulk diffraction techniques. These results will be discussed to outline the structural implications of anionic redox on both the long- and short-range ordering of the β-Li_2IrO_3 positive electrode in Li-ion batteries. This understanding will finally be used to discuss the cyclability of the anionic redox process in different voltage windows.

Methods

Synthesis

A two-step ceramic synthesis route was used to obtain pure powder of β-Li_2IrO_3. In the first step, 1 Mequiv of Iridium black (Alfa Aesar, 325 mesh, 99.9%) is mixed with 0.9 equiv of Li_2CO_3 (Sigma-Aldrich, >99%) by grinding with an agate mortar and pestle until the mixture is homogeneous. The powder is inserted into an alumina crucible covered by an alumina lid, brought to 1080 °C at 3°/min in a chamber furnace and kept for 30 h under an air atmosphere before cooling to room temperature. The resulting powder is composed of a mixture of IrO_2 and β-Li_2IrO_3. The second step is the completion of the reaction by adding 0.15 equiv of Li_2CO_3, grinding until homogeneous, and firing at 1080 °C at 3°/min for 30 h in a covered alumina crucible. The resulting powder is pure β-Li_2IrO_3 as determined by X-ray powder diffraction.

Electrochemistry

For electrochemical testing, the powders were cast into free-standing Bellcore-type electrodes by a methodology described previously.[13,24] To obtain a good signal-to-noise ratio at the Ir L_{III}-edge, the active material loading in the electrode was set to ~6 mg·cm^{-2}. Circular discs ~7 mm in diameter were used in each cell. The cycling was carried out using two electrode Swagelok-type cells with a lithium counter electrode separated from the working electrode by two layers of Whatman GF/D borosilicate glass fiber sheets soaked with a mixture of ethylene carbonate (EC), propylene carbonate (PC), and dimethyl carbonate (DMC) in a 1/1/3 weight ratio containing 1 M lithium hexafluorophosphate (LiPF6) as the electrolyte. The cells were assembled in an Ar-filled glovebox and were cycled at a C/5 rate (1 Li^+ equiv removed in 5 h) if not specified otherwise.

Hard X-ray Photoemission Spectroscopy (HAXPES)

For photoemission measurements, the electrodes were prepared by mixing the pristine material with 20 wt % carbon Super-P by ball-milling for 20 min prior to cycling, to avoid the polymer binder from disturbing the analyses. Hard X-ray photoemission spectroscopy (HAXPES) was carried out at the GALAXIES [25,26] beamline of SOLEIL synchrotron with $h\upsilon$ = 6.9 keV photon energy (third order reflection of the Si(111) double-crystal monochromator). Photoelectrons were analyzed by a SCIENTA EW4000 spectrometer, and the obtained energy resolution from the Au

Fermi edge was 0.14 eV. No charge neutralizer was used. The analysis chamber pressure was maintained around 10^{-8} mbar during the measurements. The binding energy scale was calibrated by comparison with the in-house XPS spectra carried out on the same samples.

X-ray Absorption Spectroscopy (XAS)

Ex situ XAS measurements at the iridium L_{III}-edge were carried out in the transmission mode at the ROCK beamline at the SOLEIL synchrotron in France. [27] A Si(111) channel-cut quick-XAS monochromator with an energy resolution of 2 eV at 11 keV was used. The intensity of the monochromatic X-ray beam was measured by three consecutive ionization detectors. The ex situ samples were prepared as described in the electrochemical section and never exposed to either air or moisture as described before.[28] The energy calibration was established with simultaneous absorption measurements on an iridium metal foil placed between the second and the third ionization chamber. The data was treated using the python routine described elsewhere for energy calibration and normalization.[29] The white line (WL) energy position was obtained as the zero of the first derivative of the XAS spectrum. The WL area was obtained by integrating the peak after subtracting an arctangent background as reported in our previous paper.[20] The fitting of the EXAFS oscillations was carried out using the Demeter package. The EXAFS oscillations were extracted at the Ir L_3-edge and weighted by k^3 in the k range [3.7 $Å^{-1}$ - 15.9 $Å^{-1}$]. The back-Fourier transform was done in the R-range [1 Å -3.3 Å]. All parameters except the radial distances R_i and the mean-square relative displacements σ_i^2 were fixed during the fitting procedure ($S_0^2 = 0.8$, $N_{Ir} = 3$, $N_{O1} = 6$, $N_{O2} = 24$). The value of E_0 was checked for each sample.

Diffraction

Operando X-ray powder diffraction (XRD) measurements were carried out using an airtight electrochemical cell equipped with a Be window. [30] Synchrotron XRD measurements were performed on the material science and powder diffraction (MSPD) beamline at Alba synchrotron, with a wavelength of 0.4122 Å. [31] Neutron powder diffraction (NPD) patterns for the sample at x = 0.5 were measured on a D1B high-resolution neutron two-axis powder diffractometer at the Laue–Langevin Institute, with a wavelength of 1.2882 Å.

Transmission electron microscopy (TEM)

Samples were prepared in an Ar-filled glovebox by crushing the crystals in a mortar in DMC and depositing drops of suspension onto holey carbon grids. High-angle annular dark field scanning transmission electron microscopy (HAADF-STEM) images and EDX spectra were obtained with an aberration-corrected Titan Themis Z electron microscope operated at 200 kV and equipped with a Super-X detector.

Results

To probe the contribution of Ir to the total delithiation path of β-Li_2IrO_3, ex situ samples were prepared by charging the electrodes at different potentials. The Ir L_{III}-edge XAS and more specifically the near-edge (XANES) spectra were used to follow the electronic state of Ir at selected states of charge. The Ir L_{III}-edge corresponds to transitions from $2p_{3/2}$ to empty 5d states, which lead to a large absorption peak commonly known as the white line (WL). Figure 1b shows the electrochemical voltage versus composition curve on charge of the β-Li_xIrO_3 cathode material vs Li in the half-cell configuration, together with the corresponding values of the WL energy and WL area. The cell was initially discharged to 1.35 V (x = 2.5) to observe the full Li content range from x = 2.5 to 0. The normalized XANES spectra are reported in panel c. Since the WL area depends on different parameters such as crystal-field splitting and sample crystallinity, we use the WL energy as the best indicator of the Ir oxidation state. The area of the WL is oftentimes associated with the number of empty 5d states and thus indicative of the oxidation state of Ir. However, when comparing the pristine sample's WL area to that of IrO_2, in which Ir is expected in the nominal +IV oxidation state, a large discrepancy is observed, thus ruling out this parameter to represent the electronic state of Ir.

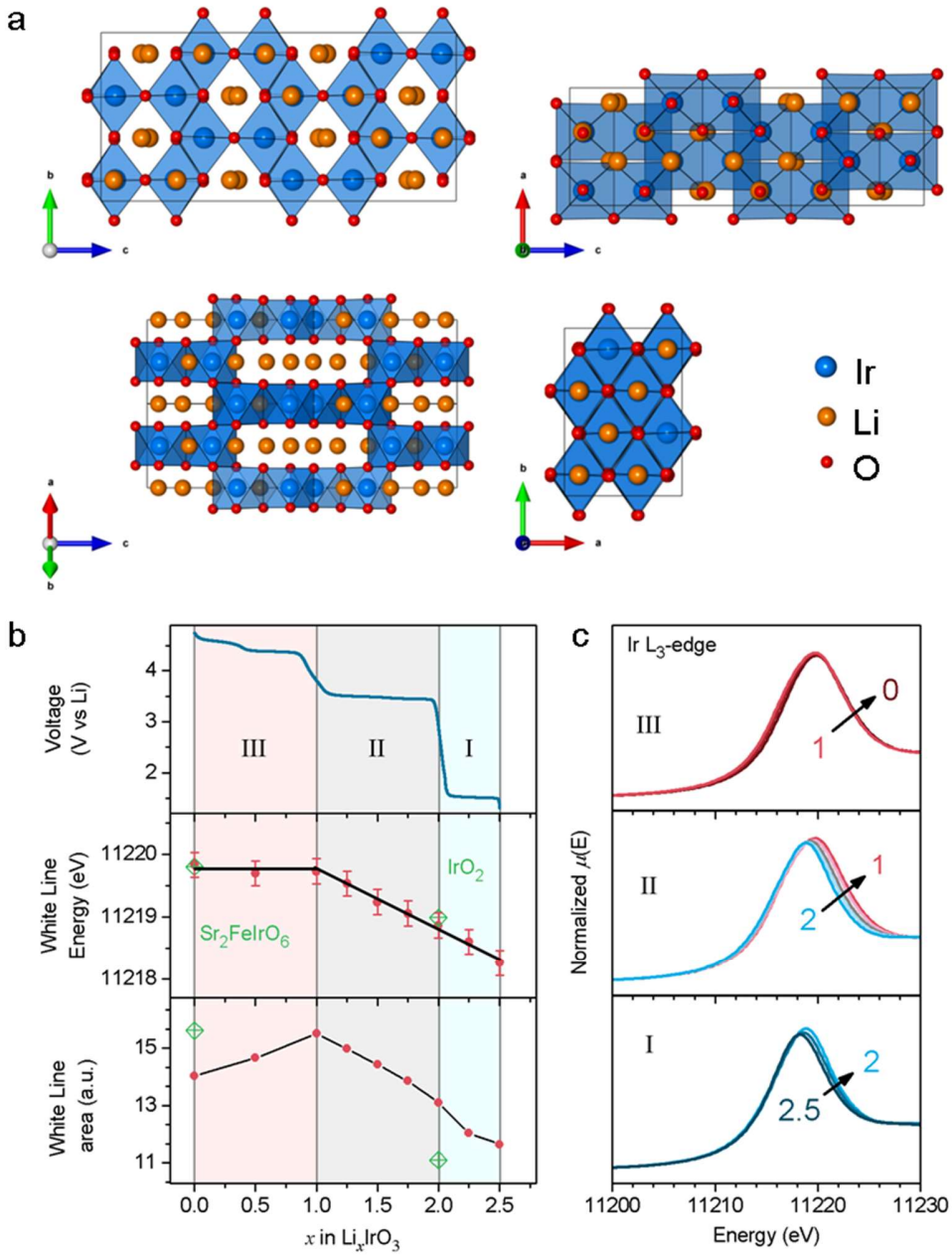

Figure 1 Structure of the β-Li_2IrO_3 compound and the electrochemical voltage versus composition curve with ex situ XANES spectra. **(a)** The structure of the material is shown along all significant directions, which are from left to right in the first row [100], [010] and [110], [001] in the second row. **(b)** The voltage profile is shown atop followed by the WL energy plot to compare the different regions labeled I, II, and III. The WL energy is correlated to the oxidation state of Ir and is determined by the point of zero crossing of the first derivative of the normalized μ(E) around the peak maximum. WL energies of two reference compounds, namely, IrO_2 and Sr_2FeIrO_6 for nominal Ir^{+IV} and Ir^{+V} states, respectively, are also shown.[32] For comparison, the peak's area is also plotted at the bottom. **(c)** The XANES spectra for ex situ samples of composition x = 2.5, 2.25, 2, 1.75, 1.5, 1.25, 1, 0.5, and 0 are shown in three different plots, which correspond to the different regimes observed in the voltage profile. As is illustrated here, Ir is mostly oxidized during segments I and II and very little during segment III.

Turning to the literature, a detailed spectral analysis of the XANES LIII edge for 5d metal oxides has been studied to determine the effect of the chemical environment, the M−O covalency, and the oxidation state on the WL shape, magnitude, and position.[33] However, numerous questions still remain regarding its exact significance.

In the case of an octahedral site, the 5d states split into t_{2g} and e_g levels according to the crystal-field theory. It has been established that the WL can be described as a sum of two Lorentzian peaks, which can be assigned to the unoccupied levels of the t_{2g} and e_g states and of an arctangent step, which describes the transitions to the continuum.[33,34] Using the second derivative considerably decreases the contribution of the step function while keeping the Lorentzian peaks intact in position and relative intensities.[35] Several examples, such as the seminal work of Choy et al. on A2BIrO6 perovskites (A = Ba, Sr, and La; B = Zn, Mr, Y, Ca, Li, and Sr), show that the peak at higher energy (the e_g states) varies linearly with the oxidation state, and recently, this was further confirmed by Laguna-Marco et al. on similar systems.[34,36,37] It is however worth noting that these perovskites have very dissimilar structures to the one studied herein. The main difference lies in the connectivity of IrO_6 octahedra. Indeed, while these octahedra are "isolated" in the case of the A_2BIrO_6 perovskite structures (sharing corners with BO_6 octahedra), they are connected through edge-sharing to three other octahedra in the hyperhoneycomb iridate. This has been observed in the aforementioned works of Choy et al. when measuring XANES on IrO_2 and $SrIrO_3$, which have interconnected IrO_6 octahedra. What they observe is that instead of seeing two distinct peaks in the second derivative of μ(E), there is only one single broad peak. This is explained by the fact that the simple vision of crystal-field splitting is insufficient in these structures and that a more complex band structure should be envisioned. Nevertheless, the peak maximum seems to align for similar oxidation states. Hence, throughout the next paragraphs, we will refer to the WL energy as the peak maximum, which is considered to shift linearly with the oxidation state.

The electrochemical curve can be described as three potential regions labeled I, II, and III in Figure 1b: the low potential process from x = 2.5 to 2 (around 1.5 V), the intermediate potential process from x = 2 to 1 (around 3.5 V), and the high potential process from x = 1 to 0 (around 4.5 V). The WL energy tends to vary linearly with composition over regions I and II. The participation of Ir in the Li^+ extraction process can therefore be described as being fairly constant over these two potential regions and consistent with a primarily cationic redox process. Indeed, as oxygen is in its most reduced state in the pristine material, the process in region I must be purely cationic.

As the oxidation of Ir is linear over regions I and II, it seems fair to say that they are both cationic in nature. However, the slope is drastically reduced in region III, which suggests that Ir is not oxidized nearly as much on the high potential plateau, implying a strong oxygen redox activity.

The oxidation state for Ir during charge can be assessed by comparing the WL energy with those of the reference compounds, showing that Ir does not exceed the +5 oxidation state. It is interesting to point out here the differences observed when comparing the WL areas of the reference compounds with those of the Li_xIrO_3 samples. As discussed above, for the same oxidation state and local environment, it would be expected to have a comparable WL area. However, the WL area corresponding to the fully charged sample is much lower than that of the reference compound in which the IrO_6 octahedra are undistorted. This discrepancy points toward the possibility of highly distorted IrO_6 octahedra in the charged phases.

As the XANES data seem to imply a strong participation of oxygen redox on charge during the high potential process, we next probed the electronic state of oxygen directly by HAXPES in ex situ samples. The use of HAXPES to probe the bulk of the material is particularly important when looking at the O 1s level because of the presence of surface contaminations (electrolyte decomposition products containing oxygen on the particle surface), which hinder the clean observation of the bulk lattice oxygen spectral components. In addition to the pristine material, the ex situ samples were prepared by charging the β-Li_2IrO_3 to different states of lithium content, namely, x = 1, 0.5, and 0. The HAXPES spectra were all measured using a photon energy of 6900 eV to increase the probe depth to ~22 nm, compared to ~4.9 nm in our previous studies using inhouse XPS (Al source, 1486.6 eV). Note that the probe depths are defined as three times the photoelectron inelastic mean free path and were estimated using the TPP-2M model.[38] The O 1s HAXPES spectra of Li_xIrO_3 with x = 2, 1, 0.5, and 0 are shown in Figure 2a. The pristine material can be described with three distinct contributions: the lattice oxygen at 529.8 eV and surface species at 531.9 and 533.5 eV. After the first Li^+ is extracted, the peak at 529.8 eV becomes asymmetric and an additional component must be introduced at 531 eV, which corresponds to what has been previously attributed to the oxidized lattice oxygen (O^{n-}, $n < 2$).[21] By plotting the area of the peak at 531 eV divided by the sum of the areas of both lattice oxygen peaks (at 529.8 and 531 eV), one can obtain a representative percentage of oxidized oxygen in the material, as shown in Figure 2b. This allows us to attribute the anionic activity not just to the second Li^+

extracted (high potential region), in good agreement with the XANES results, but also to the first lithium extraction (intermediate potential region), contradicting the XANES analysis. This disagreement is in line with the possibility of a redox coupling mechanism and the existence of a hybridized state, which is responsible for the charge compensation during delithiation. Indeed, due to the high covalence of the Ir−O bond, the redox activity is not purely cationic or anionic but rather the redox of a hybridized state described as a reductive coupling. [39] Indeed, this mechanism might not be detectable by observing the WL energy and could rather be nested in the fine structure of the near-edge region. Nevertheless, these discrepancies highlight the complicated nature of the species observed at 531 eV in the O 1s photoemission spectra and stress the need for in-depth theoretical work.

To further probe the cationic activity, the Ir 4f and 5p core levels as well as the valence band were measured by HAXPES. First, we discuss the $4f_{7/2}$-$4f_{5/2}$ as well as $5p_{3/2}$-$5p_{1/2}$ core peaks (Figure 2c). At this photon energy, the cross section of Ir 5p is non-negligible with respect to Ir 4f, and a broad contribution of $5p_{1/2}$ is necessary to fully describe the Ir 4f experimental data. This work is made easier by the known relative intensities of the different spin−orbit components: $4f_{7/2}/4f_{5/2} = 4/3$ and $5p_{3/2}/5p_{1/2} = 2$, and their known energy splitting: $4f_{5/2} - 4f_{7/2} = 3$ eV and $5p_{1/2} - 5p_{3/2} = 15$ eV. A very weak contribution of the Li 1s peak is also observed for the pristine sample at a binding energy of 55 eV, due to the low cross section of this light element. This signal is undetectable in the partially delithiated phases. During the extraction of the first Li^+ (x = 2 to 1), both the $4f_{5/2}$ and $4f_{7/2}$ peaks shift to higher binding energies, i.e., from 62.6 to 63.2 eV and from 65.6 to 66.2 eV, respectively. During the second delithiation, these peaks shift only poorly (to 63.4 and 66.4 eV, respectively), in good agreement with theXANES analysis. However, their shape changes considerably in both symmetry and width. This complex shape, including satellite peaks, is due to multielectronic photoemission processes corresponding to different final ionized states. The observed evolution is most likely symptomatic of a change in the environment of iridium, which we will come back to later in the manuscript. Taking a look at the $5p_{3/2}$ level, it is clear that there is a continuous shift toward higher binding energies from x = 2 to 0.5, but for the last 0.5 Li^+, no shift is observed. These results fully confirm the participation of Ir during the delithiation of the first Li^+, a more modest contribution to the following 0.5 Li^+ and a negligible one for the last 0.5 Li^+, in agreement with the XANES results.

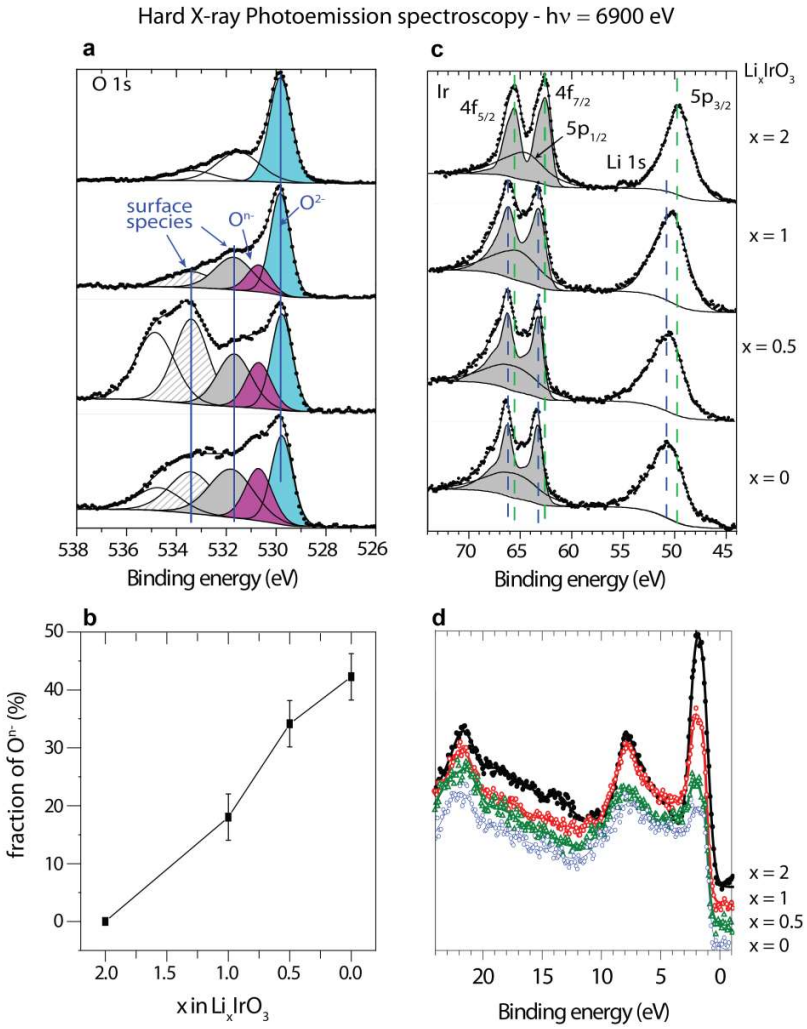

Figure 2 HAXPES results on samples of composition x = 2, 1, 0.5, and 0 with x being the amount of Li in the *β*-Li_xIrO_3. **(a)** O 1s core peaks with the blue component being the lattice O^{2-}, the pink component being the oxidized lattice oxygen named O^{n-}, and in gray, hashed, and white is the surface contamination as described previously.[2,6,21,40] **(b)** The amount of O^{n-} species normalized by the total amount of lattice oxygen at the different compositions. **(c)** Ir 4f and 5p core peaks. The gray filled area corresponds to $4f_{7/2}$ and $4f_{5/2}$ components. **(d)** HAXPES valence spectra of the material for the different Li compositions, which, at this photon energy (6900 eV), represent only the Ir 5d contribution to the occupied states.

Finally, another way to probe the participation of Ir redox in the delithiation process is by measuring the valence spectra, as shown in Figure 2d. The photoionization cross section of the Ir 5d electrons is strongly enhanced by the high incident photon energy (6900 eV) compared to O 2p electrons ($\sigma_{Ir\ 5d}/\sigma_{O\ 2p} \approx 550$) and O 2s electrons ($\sigma_{Ir\ 5d}/\sigma_{O\ 2s} \approx 17$). Hence, the measured HAXPES

valence spectrum represents purely the Ir 5d occupied density of states in the 0−11 eV region close to the Fermi level, where O 2s contributions are negligible. Consequently, the area of the valence spectrum, contrary to the XAS WL area (Figure 1b), allows us to follow directly the evolution of the Ir 5d electron and therefore to determine the Ir redox. If the area decreases, this means that there are fewer Ir 5d electrons below the Fermi energy and therefore that Ir has been oxidized; on the contrary, the area increases when Ir is reduced. In the pristine compound, the valence spectrum can be described as being composed of several broad peaks with, namely, a large peak around 2 eV, which splits into two peaks on oxidation. These peaks do not shift during oxidation, but their intensity is greatly modified. During the deintercalation of the first Li^+, the area is considerably decreased, meaning that a strong oxidation has taken place. During the following 0.5 Li^+, iridium is further oxidized but to a lesser extent, which is expected since the charge to compensate for is half that of the previous delithiation process. Finally, during the final 0.5 Li^+ extraction, Ir seems to be weakly active since the area remains almost unchanged, implying strong oxygen participation. Once again, this is in good agreement with the results described so far in this paper for the evolution of the Ir oxidation state.

To summarize, complementary spectroscopic tools have allowed us to pinpoint the different redox processes along the electrochemical curve of β-Li_xIrO_3 and evidence once again the participation of lattice oxygen in the Li extraction process. Three regimes can be spotted, for which simplified band structures are shown in Figure 3. The first one is from x = 2.5 to 2 where only Ir is redox active and responsible for the disinsertion of the 0.5 Li from the structure. The second process is from x = 2 to 1, which seems cationic in nature but during which a contribution at 531 eV to O 1s HAXPES spectra arises and which points to a remixing of the Ir and newly formed O−O states, which arise from the distortion, as described by Ben Yahia et al.39 In addition, there is the last process from x = 1 to 0, at high potential, during which Ir seems to be only slightly oxidized, if at all, and the O 1s HAXPES signal at 531 eV increases. This is again consistent with the reductive coupling mechanism although the relative contributions of Ir and O to the newly formed redox active antibonding M−(O−O)* band are inverted due to the highly oxidized state. The structural implications of such a mechanism are expected to be significant and most likely visible at both long and short ranges.

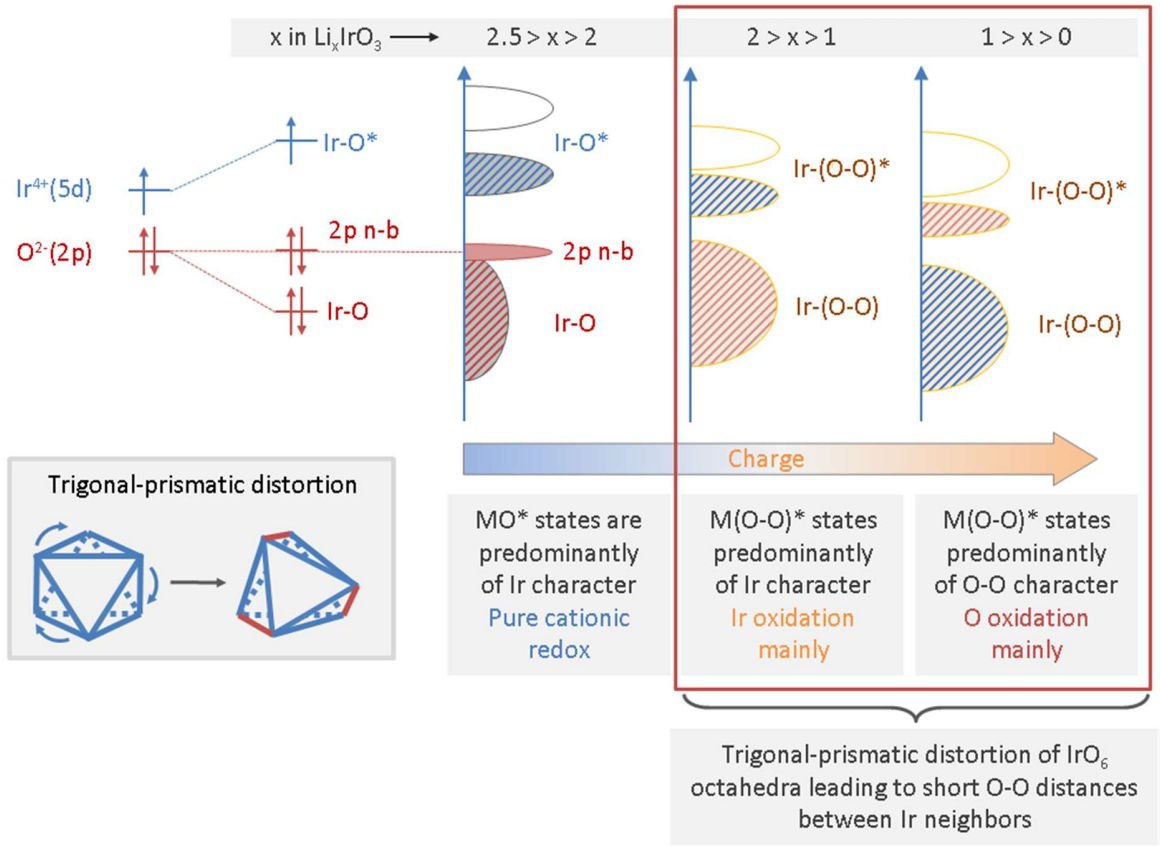

Figure 3 Evolution of the simplified band structure of the β-Li_xIrO_3 compound during charge. The hashed bands are hybridized Ir−O or Ir(O−O) states, with the color indicating the predominant character of the band (blue for Ir and red for O). The red filled band is localized only on oxygen and corresponds to the O 2p non-bonding (n-b) states. On the lower left side is shown a perfect trigonal-prismatic distortion, which should be observed with this mechanism.

Indeed, the structural changes occurring during delithiation of the β-Li_2IrO_3 phase were monitored using operando synchrotron X-ray diffraction, which was carried out between x = 2 and 0 with the voltage profile shown in Figure 4a. To improve the quality of the XRD patterns, the powder was not ball-milled with carbon, which led to a strong polarization in the first charge on the processes taking place around 3.5 V. This polarization is attributed to the large particle sizes but disappears on further cycling once 4.0 V is reached, which can be explained by electrochemical grinding. Therefore, an activation cycle was carried out by charging the material up to 4.0 V and discharging to 1.6 V to recover the pristine compound. On the curve in Figure 4a, three regions are identified (namely, A, B, and C) for which the XRD patterns are shown, respectively, in Figure 4d−f. The pristine phase can be described as an orthorhombic cell with the *Fddd* space group in

which all IrO_6 octahedra are connected to each other by edge-sharing, similar to the layered polymorph with, however, a connectivity that leads to a tridimensional framework. All phases that are formed during the delithiation could be described with either orthorhombic cells derived from the pristine material or a monoclinic distortion of the orthorhombic cell. The cell parameters could be obtained by refining the patterns using the Rietveld method as implemented in FullProf suite software, and the results are shown in Supporting Information Table S1 along with the crystallographic data in Tables S2−S8 and the refinements in Figures S1−S6. The cell volumes per formula unit as well as the phase concentration profiles obtained by the refinements are shown in Figure 4b,c. Upon removal of the first 1.15 Li^+ (Figure 4f), three successive biphasic transitions leading to orthorhombic cells with similar volumes to the pristine phase are observed. Interestingly, these intermediate phases have sharp and intense peaks, indicating that the structures are well ordered.

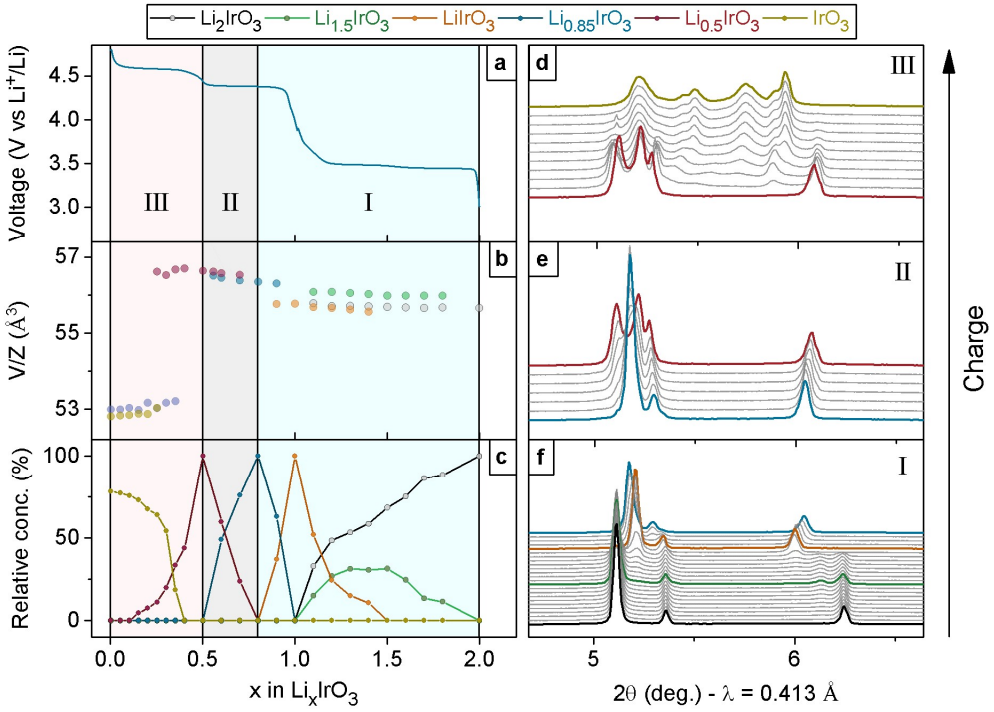

Figure 4 Operando synchrotron XRD. **(a)** Electrochemical curve of β-Li2IrO3 on charge starting from the pristine material at x = 2. **(b)** Cell volume normalized by formula unit of each intermediate phase as determined by Rietveld refinement of selected patterns. **(c)** Relative phase concentration profile. **(d)**, **(e)**, and **(f)** show the evolution of the XRD patterns during the 3-step charge

However, from x = 0.85 to 0.5, a peak splitting indicative of a monoclinic distortion with noticeable peak broadening is observed. As delithiation continues, two biphasic transitions leading to other monoclinic phases take place. The final phase can be described as a mixture of these two monoclinic phases with their β angle tending toward 90° (94.9 and 93.3°). This corresponds to a large change compared to $Li_{0.5}IrO_3$ for which $\beta \approx 105°$. The cell volume also collapses significantly in the final Li extraction process (Figure 4b). A broadening of peaks arises during this second delithiation, which is indicative of microstrain and/or of the shortening of coherent crystalline domains, which can arise from electrochemical grinding. In the first case, the broadening should be proportional to tan(θ), meaning that it should be exacerbated at wide angles, whereas, in the second case, it should be proportional to 1/cos(θ), leading to a larger effect on narrow angles. Both effects can be modeled and implemented in the refinements. This allows us to discriminate between electrochemical grinding and structural microstrain at high potential. While there seems to be a steady electrochemical grinding during charge, there is a substantial increase of anisotropic microstrain only during the second Li^+ extraction, as illustrated in Figure S7. As described above, this region can be attributed predominantly to anionic redox, and while the grinding is not exacerbated during this last Li^+ extraction, the microstrain is considerably increased. While this microstrain could coincidentally arise from the fact that a large amount of Li^+ has already been extracted at this point, it is likely due, in no minor part, to the significant distortions induced by anionic redox.

To further investigate the structural evolutions, more specifically the position of the light elements O and Li in the structure, ex situ neutron powder diffraction was carried out on the D1B neutron diffractometer at the Institut Laue Langevin in Grenoble. While the x = 1 compound was investigated in our previous work and Li found in tetrahedral sites, we focus here on the x = 0.5 composition.[6] As discussed earlier, a monoclinic distortion of the orthorhombic cell is observed at high states of charge. The monoclinic phase at x = 0.5 is described in the C2/c space group with Li being likely located in the same tetrahedral sites as the one occupied in the x = 1 composition. From x = 1 to 0.5, the symmetry is lowered from *Fddd* to *C2/c*, and the unique tetrahedral site in the *Fddd* orthorhombic structure is split in Li3a and Li3b sites in the *C2/c* space group (Figure S8). However, these two sites should be only partially occupied, so that the total stoichiometry in Li satisfies the chemical composition. To determine the exact occupancy of these two Li tetrahedral sites, simulations, with one of the two sites empty and the other one full and vice versa,

were performed and compared to the experimental data. The distinguishing feature is an inversion of relative intensities in (110) and ($\bar{1}$11) at 2θ values of 15.8 and 16.2°, respectively (Figure S8). This allows the discrimination of one of the two sites and the determination of a delithiation path. The most favorable site is the Li 3b site, which is formed by two O1 and two O2 oxygen positions. After refinement, we obtain a Li distribution of 1 for the Li 3b site and 0 for the Li 3a site, and the refinement is shown in Figure 5a with the structural parameters reported in Table S9.

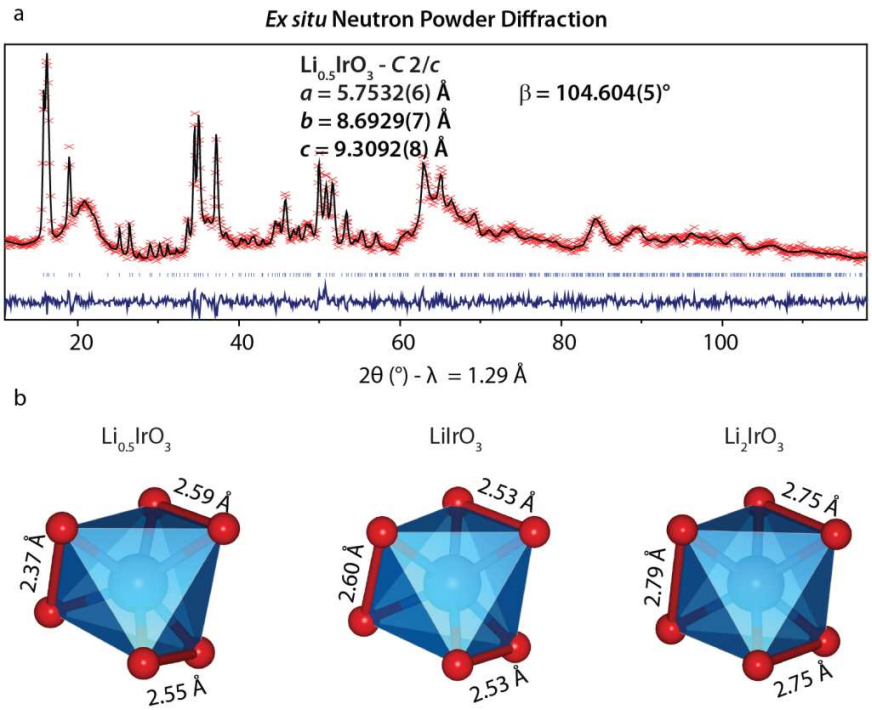

Figure 5. **(a)** Rietveld refinement of the neutron powder diffraction pattern for the $Li_{0.5}IrO_3$ structure. **(b)** IrO_6 octahedra of the different intermediates of composition x = 0.5, 1, and 2 with the short O−O distances highlighted in red and their length given in angstroms. [6]

An important consequence of anionic redox is the shortening of O−O distances, likely because two neighboring oxidized O^{n-} species stabilize by condensing as "dimers". These shortest O−O distances, which lie at the shared edge of neighboring IrO_6 octahedra, found in β-$Li_{0.5}IrO_3$ are shown in Figure 5b along with those of *β*-Li_1IrO_3 and *β*-Li_2IrO_3.[6] Interestingly, an anisotropic evolution of the O−O shortening is observed between x = 1 and 0.5, which could be an indication

of uneven participation of anions to the redox process. This goes in line with the uneven distribution of Li in the tetrahedral sites and the anisotropic microstrain observed when charging the material above 4.0 V. The shortest O−O distance falls down to 2.37(3) Å with the other two distances remaining close to that found in β-$LiIrO_3$ (2.55(5) Å). This distortion is quite different from that observed during delithiation of the first Li from the pristine material where the IrO_6 octahedra go through a trigonal-prismatic distortion with almost equivalent short O−O distances.[6] This type of distortion can be rationalized by the formation of M−(O−O) bands as has been discussed by Ben Yahia et al. for Mott−Hubbard insulators such as β-Li_2IrO_3.[39] However, it seems that beyond one Li extracted, the electronic structure tends toward the charge transfer model where the highest occupied orbitals are of O character, and a disproportionation takes place with the formation of unevenly oxidized $(O_2)^{n-}$. As the fully charged state suffers from high amounts of microstrain and therefore large broadening effects, which hinder the clear determination of the fine structure by diffraction techniques, the short-range sensitivity of the XAS technique should help clear up the high-voltage structural evolution.

For this purpose, the EXAFS oscillations extracted at their L_{III}-edge of the ex situ samples at compositions x = 2.5, 2, 1.5, 1, 0.5, and 0 were analyzed. Our fitting model is based on a first shell consisting of the first oxygen neighbors (N = 6) and the second shell consisting of the first Ir neighbors (N = 3). The contribution due to Li atoms is not taken into account because of their negligible scattering factors. Further contributions including multiple scattering were not considered, since they were not improving the fit, which are shown in Figure S9, along with the results in Table S10 of the Supporting Information. The obtained Ir−O and Ir−Ir distances and the calculated O−O distances are reported in Figure 6a; the magnitude of the Fourier transforms of the EXAFS oscillations for each intermediate is shown in Figure 6b. The O−O distances (bottom panel) were calculated using a geometric relation described previously.[28] In brief, these shorter O−O distances are located at the edge shared by two neighboring IrO_6 octahedra, such that a decrease in the Ir−O distance and/or an increase in the Ir−Ir distance led to O−O shortening.

We next describe the evolution of these distances in light of the previous observations of the charge compensation mechanism. The first section, which was attributed to $Ir^{3.5+/4+}$ redox, concerns the x = 2.5−2 composition range, which is characterized by a shortening of the Ir−O distance and also of the Ir−Ir distance, such that the O−O distances are almost invariable. This is

expected for a symmetrical contraction of the IrO_6 octahedra during which the distances should vary proportionally by the same amount (nearly the case here). This is also consistent with the previously reported NPD results6 and can be attributed to the $Ir^{3.5+/4+}$ redox process. From x = 2 to 0, all distances show a continuous and monotonous evolution with a shortening of the O−O distance from 2.75 to 2.4 Å. This is quite interesting and confirms the spectroscopic observations, which indicate a reductive coupling mechanism with the formation of M−(O−O) and M−(O−O)* states leading to a distortion of the octahedra specifically with shorter O−O distances between two Ir neighbors. However, it is important to recall that the O−O distances have been calculated based on the assumption that the distortion is somewhat symmetrical around the Ir center and that our model does not use the high-order cumulant approach and hence does not provide effective distributions of distances. [41] Nevertheless, the results and trends are very close to the average distances obtained by neutron diffraction for some compositions, as overlaid on the same figure. Another interesting observation is that the magnitudes of both Ir−O and Ir−Ir peaks in the FTs decrease as the material is charged to the highest potential (Figure S10 of the Supporting Information). This is most likely due to a certain amount of microstrain leading to some disorder even at the short range, which is in complete agreement with the XRD results.

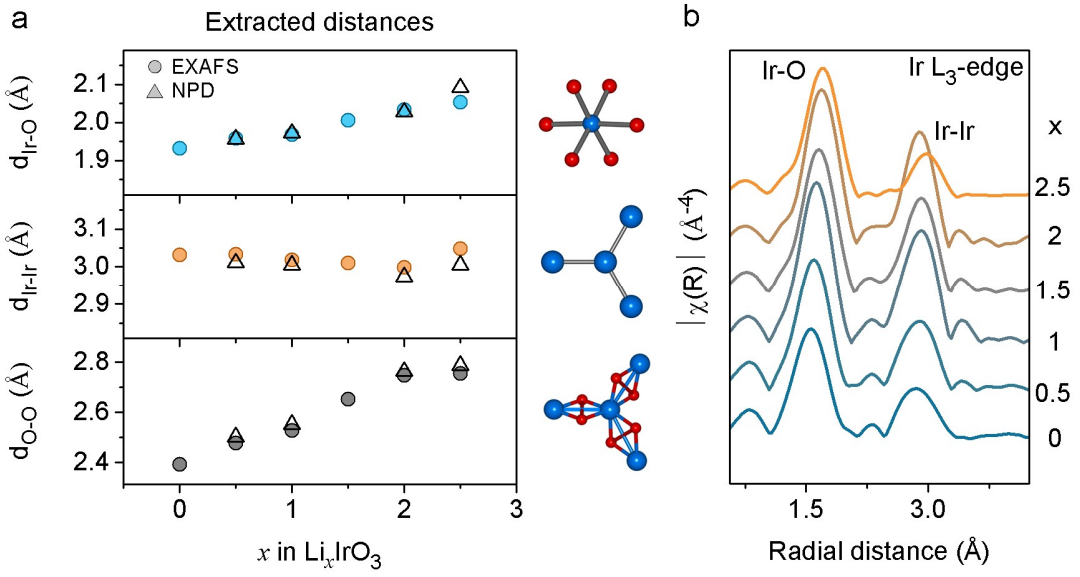

Figure 6 (a) Local distances obtained by EXAFS and compared with NPD. From top to bottom, d_{Ir-O}, d_{Ir-Ir}, and d_{O-O} are plotted. The distances obtained by NPD represented by black unfilled triangles are averaged over all distances in the cases of Ir−O and Ir−Ir and only over the three shortest ones in the case of O−O to compare with the calculated O−O distances obtained by EXAFS. **(b)** Magnitude of the Fourier transforms of the EXAFS oscillations.

While it has long been suggested that the degree of O−O distance shortening is a measure of the amount of anionic redox, these results suggest that it might not be straightforward to use average distances to differentiate cationic and anionic redox processes, especially in the case of a reductive coupling mechanism. Similarly, the question of quantification of anionic participation remains delicate in situations where both lattice oxygen and transition metal are involved.

Implication of anionic redox on cycling stability

It has been previously demonstrated that the hyperhoneycomb iridate has a staircase profile on first charge, which is retained on the subsequent discharge and maintained for several cycles before being modified.[6] While this is also the case for its layered counterpart, [42] full delithiation is possible here, and an IrO_3 phase can be obtained with a considerable amount of oxygen participation in the redox processes at both low and high potentials for $x < 2$. The degree of participation of oxygen is however not uniform throughout the charge and more specifically on the last 0.5 Li^+. To better understand the effects of this increasing anionic participation on cycling, the voltage profiles of cells cycled between 2.0 and 4.0 V (cell A), 4.45 V (cell B), or 4.8 V (cell C) at a rate of C/5 over ten cycles are shown in Figure 7, along with the associated derivative curves in panel b. While cell A shows perfect reversibility over the 10 first cycles with no modification of the profile or any voltage fade, this is not the case for cells B and C. Indeed, in the case of cell B, after 10 cycles, the profile shows significant changes, namely, the apparition of a slopelike region between the low- and high-voltage plateaus and also a slight voltage fade on the low-voltage process as seen from the derivative curve. Interestingly, the high potential plateau at 4.4 V seems to retain its voltage and displays negligible hysteresis considering the fact that oxygen participation is significant at this potential. But it is only when the process at 4.8 V is achieved that significant modifications to the electrochemical profile and voltage fade are observed on all plateaus.

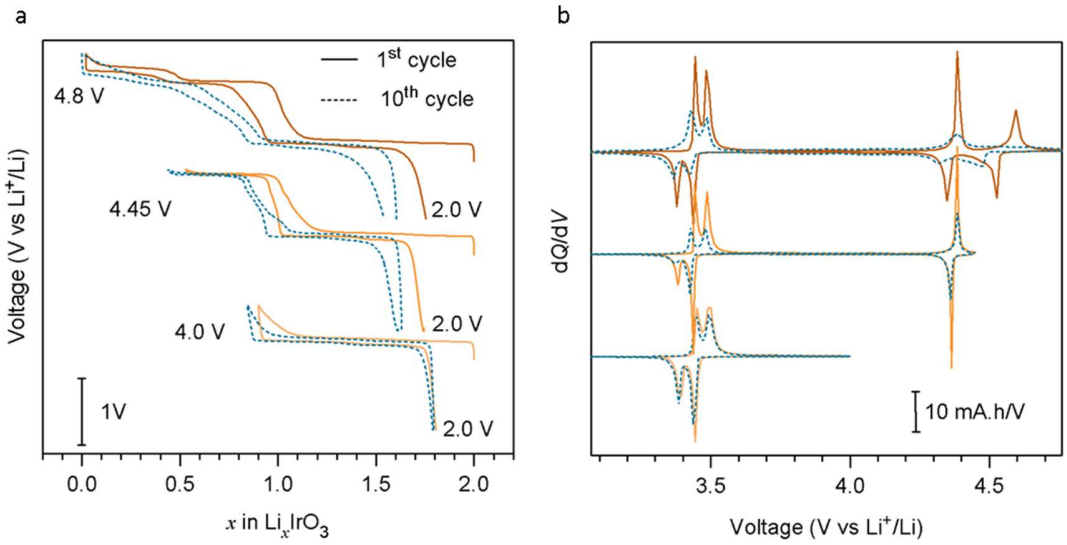

Figure 7 (a) Voltage composition curves of different cells cycled at C/5 up to different high-voltage cutoff potentials with the first cycle in orange and the 10th cycle in dashed blue. **(b)** Associated derivative curves.

Generally, this type of voltage curve modification over cycling has been attributed to cation migrations in the Li-rich layered materials. To trace possible migrations of the Ir cations to the Li sites upon repetitive charge−discharge at different upper voltage thresholds, a scanning transmission electron microscopy investigation of the electrodes cycled 10 times in the 2.0−4.0 and 2.0−4.8 V ranges was undertaken. The representative HAADF-STEM images in Figure 8 demonstrate well-ordered hyperhoneycomb arrangements of the Ir cations characteristic of the *β*-Li_2IrO_3 structure. Traces of the HAADF intensity across the Ir and Li 16d positions of the *Fddd* crystal structure indicate that the Ir cations either do not migrate to the Li sites or this migration is fully reversible at both voltage windows. Nanosized Ir clusters are present at the surface of the crystallites in the sample cycled between 2.0 and 4.8 V. Depletion of these nanoclusters with oxygen is evident from the EDX compositional map in Figure S11 of the Supporting Information. The formation of these nanoclusters might be related to some minor oxygen release or electrolyte oxidation when the electrode is charged to 4.8 V.

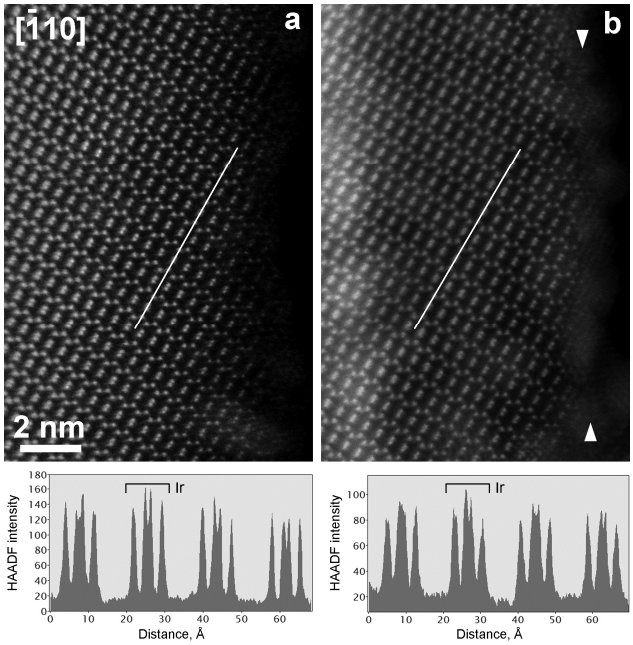

Figure 8 Comparison of the atomic structure of β-Li_2IrO_3 cycled between 2.0 and 4.0 V (a) and 2.0 and 4.8 V (b). The HAADF intensity profiles are plotted along the lines marked in the images crossing the Ir and Li 16d positions of the *Fddd* crystal structure. The peaks on the profiles are assigned exclusively to the Ir 16d position (marked with brackets), indicating the absence of the Ir migration to the Li sites. The surface of the sample cycled between 2.0 and 4.8 V is decorated with Ir nanoclusters (marked with arrowheads).

It is clear that the microstrain imposed on the structure by the uneven and short O−O distances observed by NPD and EXAFS has an adverse impact on the electrochemical behavior. In addition, the redox active band shifting to a predominantly (O−O) character, as depicted in a simplified band diagram in Figure 3, could be the cause of such a modification of the electrochemical behavior, namely, through the formation of even a small amount of oxygen vacancies due to oxygen release. However, this has yet to be confirmed through additional DEMS experiments. Theoreticians have suggested that only 0.33 e^- can be reversibly taken per oxygen atom before observing an irreversibility in the process.[39] In the case of IrO_3, as Ir does not exceed the +5 oxidation state, 1 e^- is taken per three lattice oxygens, making it very close to this theoretical limit. This could therefore explain the considerable observed instability.

Conclusion

The use of complementary synchrotron X-ray and neutron spectroscopic and diffraction techniques has enabled us to probe the degree of participation of both the lattice oxygen and iridium in the delithiation process of the β-Li_2IrO_3 framework as well as the structural implications of the resulting reductive coupling mechanism. We have observed several distinct redox and structural evolution regimes during charge, namely, (I) a pure cationic regime with biphasic and unstrained structural changes between x = 2.5 and 2, (II) the formation of a hybridized M-(O−O)* state, which is located on Ir between x = 2 and x ≈ 0.85 with smooth biphasic transitions and negligible microstrain, followed by (III) an inversion of the respective weights of Ir and (O−O) in the hybridized state for x < 0.85. We show that while a continuous distortion is observed from x = 2 to 0 with the shortening of the O−O distances between neighboring Ir (corresponding to a trigonal-prismatic distortion), the high potential process leads to strain and disorder at both long and short ranges. Indeed, as the redox active band tends toward a predominantly (O−O) character, a monoclinic distortion with increasing microstrain and uneven shortening of O−O distances arises. Pushing this mechanism to a limit of 0.33 e^- per O seems to be at the origin of the unstable electrochemical behavior when cycling repetitively up to 4.8 V. While the migration of Ir to the Li site has been discarded as a reason for this behavior as evidenced by the TEM analysis, the compounded release of oxygen over cycling would lead to the formation of oxygen vacancies as suggested by the formation of Ir nanoclusters on the surface of the particles. In turn, this could result in the observed modification of the voltage profile. Thus far, minimizing the number of holes on the anion has shown improvement in cyclability and voltage retention. We believe this study brings accurate experimental evidence of a previously described mechanism involving both cations and anions using a suite of X-ray spectroscopies and diffraction. It is evident that more work must be carried out to clarify the nature of the XPS photoemission signal appearing at 531 eV when oxygen is involved in the charge compensation mechanism. Further studies using RIXS along with in-depth theoretical support should prove useful to further elaborate on the nature of the oxidized oxygen species formed during charge in such compounds.

Acknowledgements

The authors would like to thank Matthieu Saubanère for the fruitful discussions around the theoretical aspects of anionic redox and the reductive coupling mechanism. J.-M. Tarascon acknowledges funding from the European Research Council (ERC) (FP/2014)/ERC Grant-Project 670116-ARPEMA. This work is based on experiments performed on the Materials Science and Powder Diffraction Beamline at ALBA synchrotron (proposal number 2016091814), Cerdanyola del Vallès, E-08290 Barcelona, Spain. The neutron powder diffraction experiment was performed on the D1B neutron diffractometer at the Institut Laue Langevin, Grenoble, France, and the authors would like to thank Vivian NASSIF for her help during the experiment. The XAS experiments were performed on the ROCK beamline at SOLEIL synchrotron (proposal number 20171299), which is benefiting from a public grant overseen by the French National Research Agency as part of the "Investissements d'Avenir" program (Reference: ANR-10-EQPX-45). The authors would like to thank J. Ablett and J.-P. Rueff for their assistance during the HAXPES experiment performed on the GALAXIES beamline at SOLEIL synchrotron (proposal number 0171035). The access to TEM is provided by AICF of Skoltech.

Supplementary information

Anionic and Cationic Redox Processes in β-Li_2IrO_3 and Their Structural Implications on Electrochemical Cycling in a Li-Ion Cell

Paul E. Pearce[1,2,3,‡], Gaurav Assat[1,2,3,‡], Antonella Iadecola[2], François Fauth[4], Rémi Dedryvère[2,5], Artem Abakumov,[6] Gwenaëlle Rousse[1,2,3] and Jean-Marie Tarascon[1,2,3]*

[1]Collège de France, Chimie du Solide et de l'Energie, UMR 8260, 11 Place Marcelin Berthelot, 75231 Paris Cedex 05, France.
[2]Réseau sur le Stockage Electrochimique de l'Energie (RS2E), FR CNRS 3459, 80039 Amiens Cedex, France.
[3]Sorbonne Université, 4 Place Jussieu, F-75005 Paris, France.
[4]CELLS - ALBA synchrotron, Cerdanyola del Valles, Barcelona E-08290, Spain
[5]IPREM, CNRS, Université de Pau & Pays Adour, E2S-UPPA, Hélioparc, 2 Avenue P. Angot, 64053 Pau Cedex 9, France
[6]Skoltech Center for Energy Science and Technology, Skolkovo Institute of Science and Technology, Moscow 121205, Russian Federation

‡ These authors contributed equally.

* Correspondence with: jean-marie.tarascon@college-de-france.fr

Table S 1 Space group and unit cell parameters of the β-Li_xIrO_3 (x = 2, 1.5, 1, 0.5 and 0) phases as obtained from Rietveld refinement of the operando synchrotron data.

Composition	Space group	*a* (Å)	*b* (Å)	*c* (Å)	*β* (°)	Vol (Å^3)
Li_2IrO_3	*F d d d*	5.90709(7)	8.45673(9)	17.82780(17)	90	890.543(18)
$Li_{1.5}IrO_3$	*F d d d*	5.8279(3)	8.6685(4)	17.7380(9)	90	896.11(7)
Li_1IrO_3	*F d d d*	5.61885(6)	8.87546(9)	17.8926(3)	90	892.300(18)
$Li_{0.85}IrO_3$	*F d d d*	5.69115(15)	8.77962(17)	18.0435(4)	90	901.50(4)
$Li_{0.5}IrO_3$	*C 2/m*	5.73738(20)	8.71946(19)	9.36504(18)	104.6815(14)	453.207(20)
IrO_3	*C 2/m*	5.3493(4)	9.0662(3)	8.7203(4)	93.200(5)	422.26(4)
	C 2/m	5.2822(4)	9.1414(4)	8.8473(5)	94.882(7)	425.66(4)

Table S 2 Crystallographic data and atomic positions of β-Li_2IrO_3 determined from Rietveld refinement of the *operando* synchrotron data.

β-Li_2IrO_3

Space group *F d d d* R_{Bragg} = 6.83 % χ^2 = 10.91

a = 5.90709(7) Å *b* = 8.45673(9) Å *c* = 17.82779(16) Å V = 890.581(16) Å^3

Atom	Wyckoff position	*x/a*	*y/b*	*z/c*	Occupancy	B (Å^2)
Ir	16*g*	1/8	1/8	0.70824(8)	1	0.38(2)
Li1	16*g*	1/8	1/8	0.04167	1	1
Li2	16*g*	1/8	1/8	0.875	1	1
O1	16*e*	0.850(4)	1/8	1/8	1	0.64(14)
O2	32*h*	0.647(4)	0.3644(11)	0.0372(6)	1	0.64(14)

Table S 3 Crystallographic data and atomic positions of β-$Li_{1.5}IrO_3$ determined from Rietveld refinement of the *operando* synchrotron data.

β-$Li_{1.5}IrO_3$

Space group *F d d d* R_{Bragg} = 5.12 % χ^2 = 9.83

a = 5.8279(3) Å *b* = 8.6685(4) Å *c* = 17.7380(9) Å V = 896.11(7) Å^3

Atom	Wyckoff position	*x/a*	*y/b*	*z/c*	Occupancy	B (Å^2)
Ir	16*g*	1/8	1/8	0.70824(8)	1	0.38(2)
Li1	16*g*	1/8	1/8	0.04167	1	1
Li2	16*g*	1/8	1/8	0.875	1	1
O1	16*e*	0.850	1/8	1/8	1	1
O2	32*h*	0.647	0.3644	0.0372	1	1

Table S 4 Crystallographic data and atomic positions of β-Li_1IrO_3 determined from Rietveld refinement of the *operando* synchrotron data.

β-$LiIrO_3$

Space group *F d d d* R_{Bragg} = 5.96 % χ^2 = 12.1

a = 5.61885(6) Å *b* = 8.87546(9) Å *c* = 17.8926(3) Å V = 892.300(18) Å^3

Atom	Wyckoff position	*x/a*	*y/b*	*z/c*	Occupancy	B (Å^2)
Ir	16*g*	1/8	1/8	0.70892(9)	1	0.50(2)
Li3	16*g*	1/8	0.973200	1/8	1	1
O1	16*e*	0.8566	1/8	1/8	1	1
O2	32*h*	0.6288	0.34651	0.03538	1	1

Table S 5 Crystallographic data and atomic positions of β-$Li_{0.85}IrO_3$ determined from Rietveld refinement of the *operando* synchrotron data.

β-$Li_{0.85}IrO_3$

Space group *F d d d* R_{Bragg} = 8.74 % χ^2 = 14.8

a = 5.69115(15) Å *b* = 8.77962(17) Å *c* = 18.0435(4) Å V = 901.50(4) Å^3

Atom	Wyckoff position	*x/a*	*y/b*	*z/c*	Occupancy	B (Å^2)
Ir	16*g*	1/8	1/8	0.70788(10)	1	0.77(4)
Li3	16*g*	1/8	0.973200	1/8	0.85	1
O1	16*e*	0.8566	1/8	1/8	1	1
O2	32*h*	0.6288	0.34651	0.03538	1	1

Table S 6 Crystallographic data and atomic positions of β-$Li_{0.5}IrO_3$ determined from Rietveld refinement of the *operando* synchrotron data.

β-$Li_{0.5}IrO_3$

Space group *C 2/m* R_{Bragg} = 5.89 % χ^2 = 10.00

a = 5.73738(20) Å *b* = 8.71946(19) Å *c* = 9.36504(18) Å β = 104.6815(14)° V = 453.207(20) Å^3

Atom	Wyckoff position	*x/a*	*y/b*	*z/c*	Occupancy	B (Å^2)
Ir	8*f*	0.0814(3)	0.3706(2)	0.41577(19)	1	0.46(3)
Li3b	4*c*	0.5	0.771910	0.75	0.5	1
O1	8*f*	0.208060	0.365940	0.245430	1	1
O2	8*f*	0.412510	0.094730	0.076140	1	1
O3	8*f*	0.094880	0.151200	0.449710	1	1

Table S 7 Crystallographic data and atomic positions of β-IrO_3 phase 1 determined from Rietveld refinement of the *operando* synchrotron data.

β-IrO_3 phase 1

Space group *C 2/m* R_{Bragg} = 6.56 % χ^2 = 4.29

a = 5.3493(4) Å *b* = 9.0662(3) Å *c* = 8.7203(4) Å β = 93.200(5)° V = 422.26(4) Å^3

Atom	Wyckoff position	*x/a*	*y/b*	*z/c*	Occupancy	B (Å^2)
Ir	8*f*	0.0883(7)	0.3645(3)	0.4171(3)	1	1.060(13)
O1	8*f*	0.208060	0.365940	0.245430	1	1
O2	8*f*	0.412510	0.094730	0.076140	1	1
O3	8*f*	0.094880	0.151200	0.449710	1	1

Table S 8 Crystallographic data and atomic positions of β-IrO_3 phase 2 determined from Rietveld refinement of the *operando* synchrotron data.

β-IrO_3 phase 2

Space group *C 2/m* R_{Bragg} = 4.53 % χ^2 = 4.29

a = 5.2822(4) Å *b* = 9.1414(4) Å *c* = 8.8473(5) Å β = 94.882(7)° V = 425.66(4) Å^3

Atom	Wyckoff position	*x/a*	*y/b*	*z/c*	Occupancy	B (Å^2)
Ir	8*f*	0.0720(9)	0.3697(5)	0.4231(4)	1	1.060(13)
O1	8*f*	0.208060	0.365940	0.245430	1	1
O2	8*f*	0.412510	0.094730	0.076140	1	1
O3	8*f*	0.094880	0.151200	0.449710	1	1

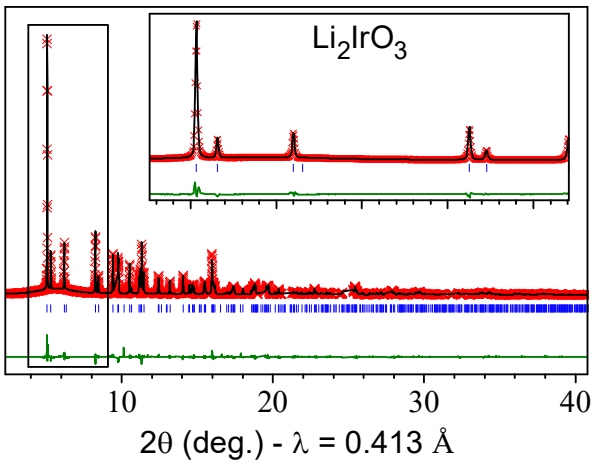

Figure S 1 Rietveld refinement of the *in situ* Synchrotron X-ray diffraction patterns for β-Li_2IrO_3. In red are the experimental points, in black is the calculated pattern and in green is the difference between the experimental and calculated patterns. The vertical blue ticks beneath the pattern indicate the positions of the Bragg reflections.

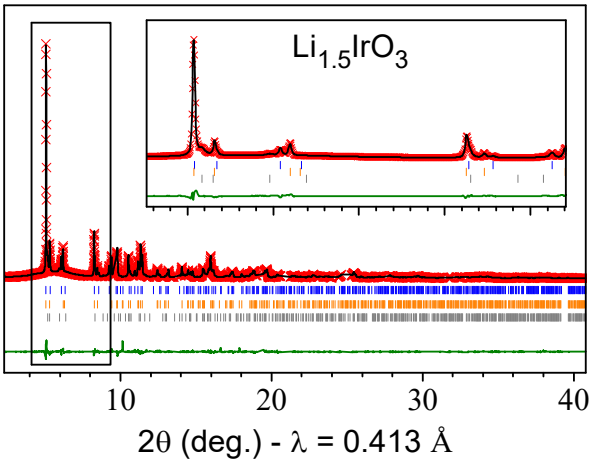

Figure S 2 Rietveld refinement of the *in situ* Synchrotron X-ray diffraction patterns for β-$Li_{1.5}IrO_3$. In red are the experimental points, in black is the calculated pattern and in green is the difference between the experimental and calculated patterns. The vertical blue ticks beneath the pattern indicate the positions of the Bragg reflections. This refinement was carried out using three phases of composition x = 2, 1.5 and 1 which are shown by the blue, orange and grey ticks respectively.

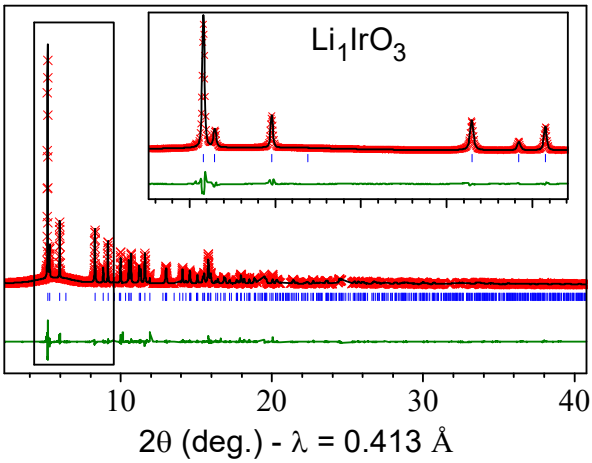

Figure S 3 Rietveld refinement of the *in situ* Synchrotron X-ray diffraction patterns for β-Li_1IrO_3. In red are the experimental points, in black is the calculated pattern and in green is the difference between the experimental and calculated patterns. The vertical blue ticks beneath the pattern indicate the positions of the Bragg reflections.

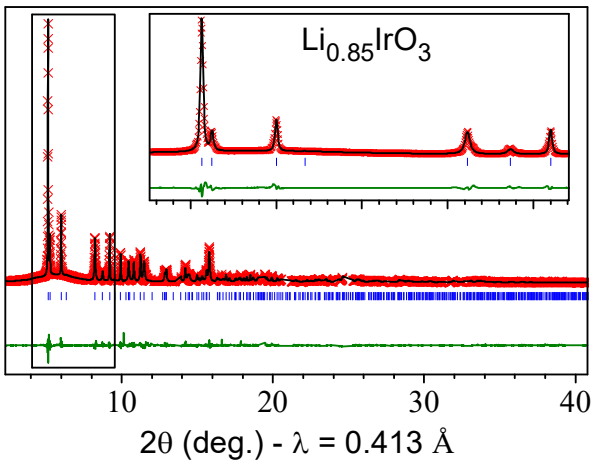

Figure S 4 Rietveld refinement of the *in situ* Synchrotron X-ray diffraction patterns for β-$Li_{0.5}IrO_3$. In red are the experimental points, in black is the calculated pattern and in green is the difference between the experimental and calculated patterns. The vertical blue ticks beneath the pattern indicate the positions of the Bragg reflections.

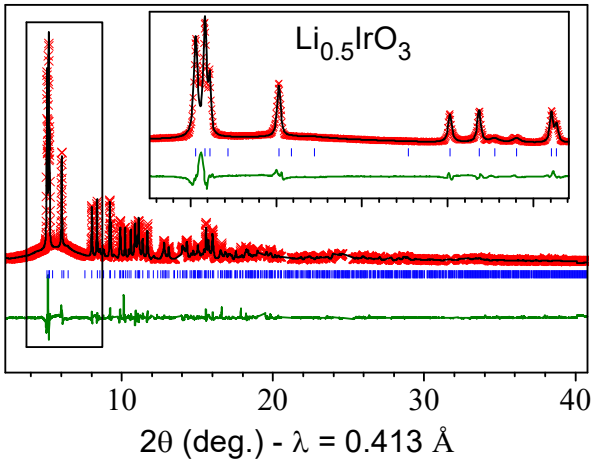

Figure S 5 Rietveld refinement of the *in situ* Synchrotron X-ray diffraction patterns for β-$Li_{0.35}IrO_3$. In red are the experimental points, in black is the calculated pattern and in green is the difference between the experimental and calculated patterns. The vertical blue ticks beneath the pattern indicate the positions of the Bragg reflections.

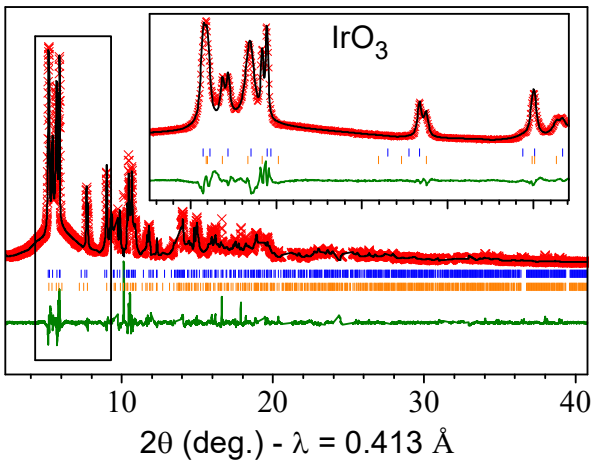

Figure S 6 Rietveld refinement of the *in situ* Synchrotron X-ray diffraction patterns for β-IrO_3 which was only obtained as a mixture of two phases of compositions x = 0.35 and 0, in orange and blue respectively. In red are the experimental points, in black is the calculated pattern and in green is the difference between the experimental and calculated patterns. The vertical blue ticks beneath the pattern indicate the positions of the Bragg reflections. The blue and orange ticks correspond to the phases 2 and 1 respectively.

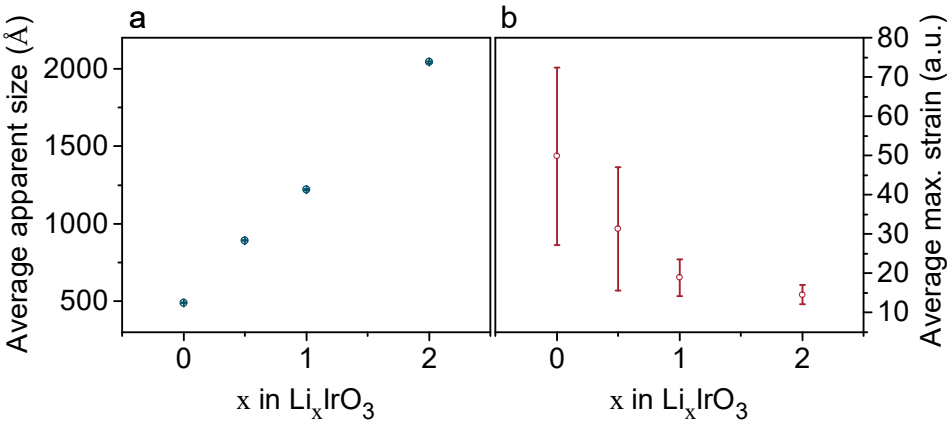

Figure S 7 Broadening parameters obtained from Rietveld refinements. a) The average apparent size which is determined by a lorentzian broadening varying in 1/cosθ. b) The average maximum strain obtained by both Gaussian and Lorentzian broadening varying in tanθ. The large standard deviation at high states of charge for the strain is due to its anisotropic nature.

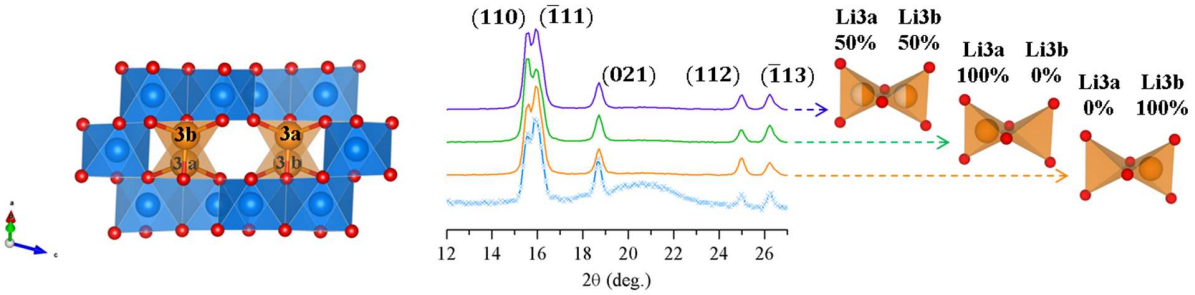

Figure S 8 Characteristic structure view (left) with Ir in blue, O in red and Li in orange. Experimental data in light blue, simulations for Li3b full and Li3a empty in orange, Li3a full and Li3b empty in green and both sites statistically filled in purple.

Table S 9 Crystallographic data and atomic positions of β-$Li_{0.5}IrO_3$ determined from Rietveld refinement of its neutron diffraction pattern.

β-$Li_{0.5}IrO_3$

Space group *C* 2/*c*			R_{Bragg} = 4.45 %		χ^2 = 23.71	
a = 5.7532(6) Å	*b* = 8.6929(7) Å	*c* = 9.3092(8) Å	β = 104.604(5)°		V = 450.53(7) Å^3	
Atom	Wyckoff position	*x/a*	*y/b*	*z/c*	Occupancy	B (Å^2)
Ir	8*f*	0.0823(15)	0.3661(11)	0.4164(9)	1	1.33(14)
Li3b	4*c*	1/2	3/4	3/4	0.5	2(2)
O1	8*f*	0.2045(18)	0.365(2)	0.2451(10)	1	0.93(11)
O2	8*f*	0.402(2)	0.0937(15)	0.0751(13)	1	0.93(11)
O3	8*f*	0.091(2)	0.1484(19)	0.4509(12)	1	0.93(11)

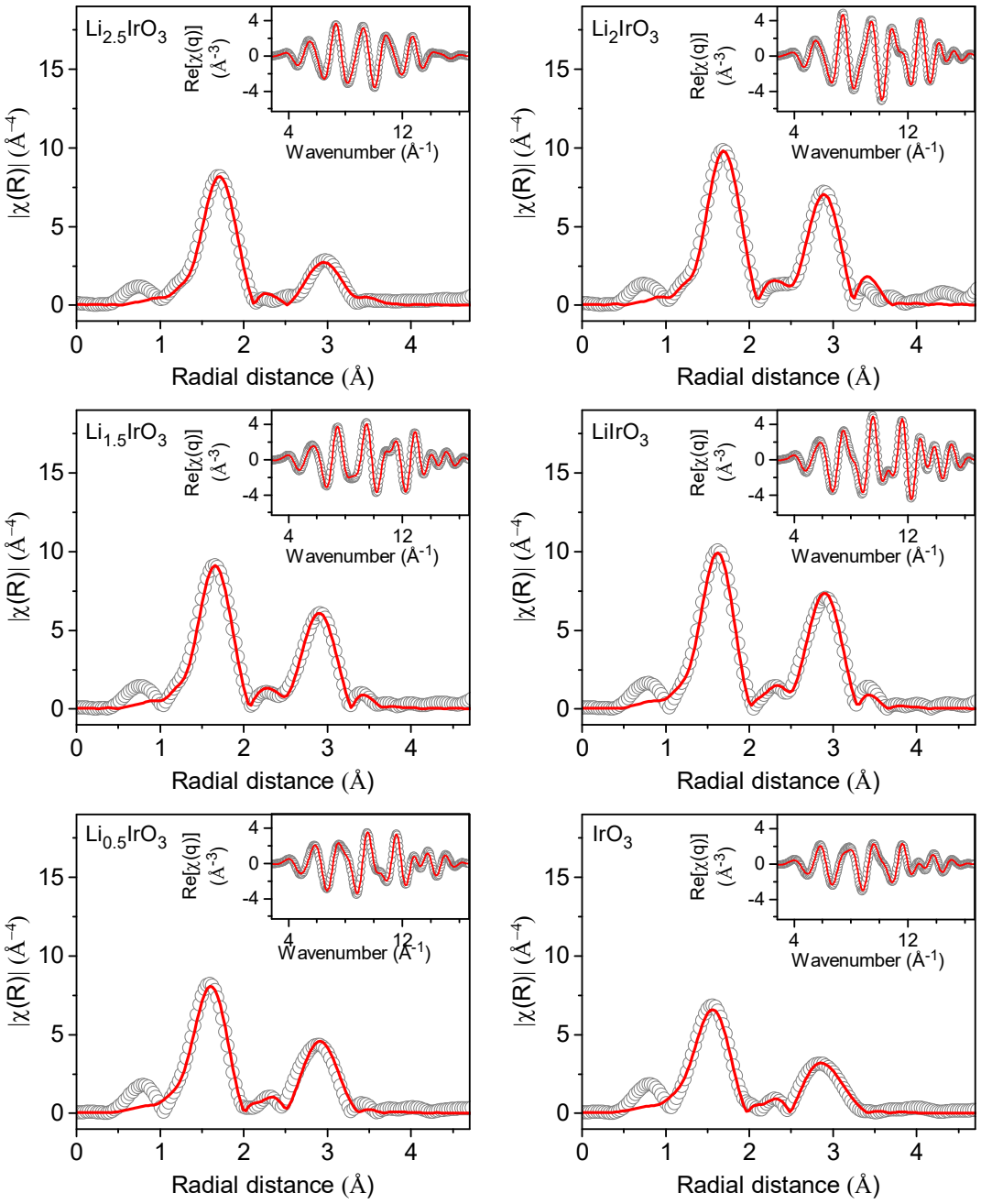

Figure S 9 Magnitude of the Fourier transform of k^3-weighted EXAFS oscillations for samples of compositions x = 2.5, 2, 1.5, 1, 0.5 and 0 (with x in Li_xIrO_3) along with the fitting results in both R- and q-space (The |χ(R)| plots were not corrected for phase shifts).

Table S 10 Fitting results of EXAFS measured on ex situ samples at different lithium contents for β-Li_2IrO_3.

x	IrO_6 (first shell)			$IrIr_3$ (second shell)			Calculated O-O distance (Å)
	CN	*R* (Å)	σ^2 (Å^2)	CN	*R* (Å)	σ^2 (Å^2)	
2.5	6	2.054 (2)	0.0033 (2)	3	3.047 (4)	0.0068 (3)	2.754 (4) R-factor = 0.0118
2	6	2.033 (1)	0.0024 (1)	3	2.998 (1)	0.00291 (8)	2.746 (2) R-factor = 0.0031
1.5	6	2.006 (2)	0.0030 (2)	3	3.010 (1)	0.0035 (1)	2.652 (2) R-factor = 0.0040
1	6	1.968 (2)	0.0026 (2)	3	3.018 (2)	0.0026 (1)	2.528 (3) R-factor = 0.0077
0.5	6	1.958 (1)	0.0039 (5)	3	3.034 (3)	0.0043 (3)	2.476 (3) R-factor = 0.0160
0	6	1.930 (2)	0.005 (2)	3	3.030 (2)	0.0053 (2)	2.391 (3) R-factor = 0.0164

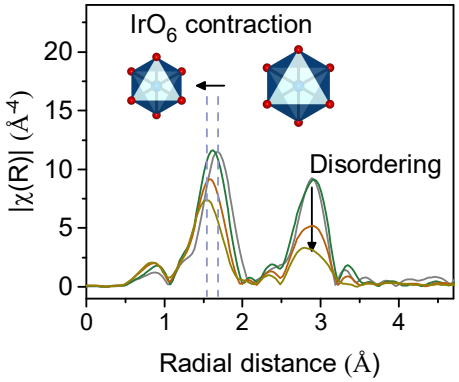

Figure S 10 Magnitude of the Fourier transform of k^3-weighted EXAFS oscillations for samples of compositions *x* = 2.5, 2, 1.5, 1, 0.5 and 0 (with *x* in Li_xIrO_3) showing the shift in the first shel and the broadening of the peaks.

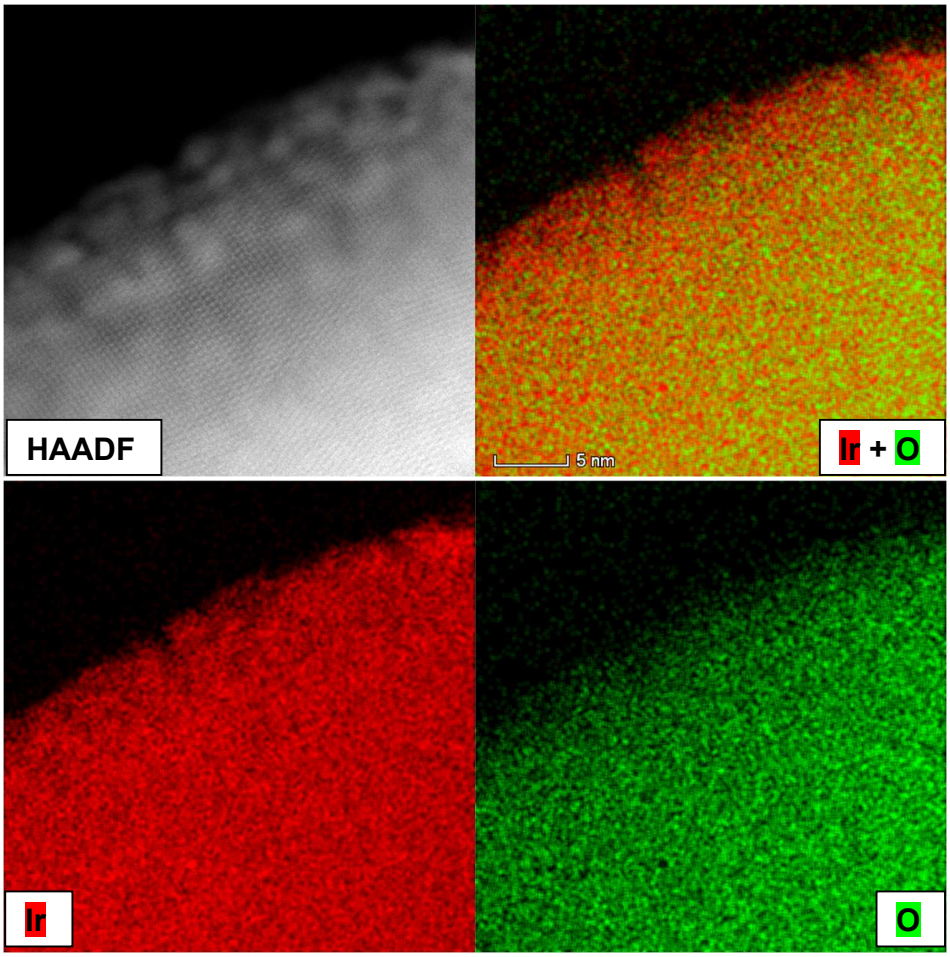

Figure S 11 HAADF-STEM image, Ir and O EDX compositional maps and the color-coded mixed map of the surface nanoclusters in the sample cycled between

References

[1] Assat, G.; Tarascon, J.-M., Fundamental Understanding and Practical Challenges of Anionic Redox Activity in Li-Ion Batteries. *Nat. Energy* 2018, 3, 373−386

[2] Sathiya, M.; Ramesha, K.; Rousse, G.; Foix, D.; Gonbeau, D.; Prakash, A. S.; Doublet, M. L.; Hemalatha, K.; Tarascon, J.-M. High Performance $Li_2Ru_{1-y}Mn_yO_3$ ($0.2 \leq y \leq 0.8$) Cathode Materials for Rechargeable Lithium-Ion Batteries: Their Understanding. *Chem. Mater.* 2013, 25, 1121−1131.

[3] Sathiya, M.; Rousse, G.; Ramesha, K.; Laisa, C. P.; Vezin, H.; Sougrati, M. T.; Doublet, M.-L.; Foix, D.; Gonbeau, D.; Walker, W.; et al. Reversible Anionic Redox Chemistry in High-Capacity Layered-Oxide Electrodes. *Nat. Mater.* 2013, 12, 827−835

[4] Sathiya, M.; Abakumov, A. M.; Foix, D.; Rousse, G.; Ramesha, K.; Saubanère, M.; Doublet, M. L.; Vezin, H.; Laisa, C. P.; Prakash, A. S.; et al. Origin of Voltage Decay in High-Capacity Layered Oxide Electrodes. *Nat. Mater.* 2015, 14, 230−238

[5] McCalla, E.; Abakumov, A. M.; Saubanère, M.; Foix, D.; Berg, E. J.; Rousse, G.; Doublet, M.-L.; Gonbeau, D.; Novák, P.; Van Tendeloo, G.; et al. Visualization of O-O Peroxo-like Dimers in High-Capacity Layered Oxides for Li-Ion Batteries. *Science* 2015, 350, 1516−1521.

[6] Pearce, P. E.; Perez, A. J.; Rousse, G.; Saubanère, M.; Batuk, D.; Foix, D.; McCalla, E.; Abakumov, A. M.; Van Tendeloo, G.; Doublet, M.-L.; et al. Evidence for Anionic Redox Activity in a Tridimensional-Ordered Li-Rich Positive Electrode β-Li_2IrO_3. *Nat. Mater.* 2017, 16, 580−586.

[7] Hong, J.; Gent, W. E.; Xiao, P.; Lim, K.; Seo, D.-H.; Wu, J.; Csernica, P. M.; Takacs, C. J.; Nordlund, D.; Sun, C.-J.; et al. Metal-Oxygen Decoordination Stabilizes Anion Redox in Li-Rich Oxides. *Nat. Mater.* 2019, 18, 256−265

[8] Assat, G.; Foix, D.; Delacourt, C.; Iadecola, A.; Dedryvère, R.; Tarascon, J.-M. Fundamental Interplay between Anionic/Cationic Redox Governing the Kinetics and Thermodynamics of Lithium-Rich Cathodes. *Nat. Commun.* 2017, 8, 2219

[9] Seo, D.-H.; Lee, J.; Urban, A.; Malik, R.; Kang, S.; Ceder, G. The Structural and Chemical Origin of the Oxygen Redox Activity in Layered and Cation-Disordered Li-Excess Cathode Materials. *Nat. Chem.* 2016, 8, 692−697

[10] Koga, H.; Croguennec, L.; Ménétrier, M.; Douhil, K.; Belin, S.; Bourgeois, L.; Suard, E.; Weill, F.; Delmas, C. Reversible Oxygen Participation to the Redox Processes Revealed for $Li_{1.20}Mn_{0.54}Co_{0.13}Ni_{0.13}O_2$. *J. Electrochem. Soc.* 2013, 160, A786-A792.

[11]Oishi, M.; Yogi, C.; Watanabe, I.; Ohta, T.; Orikasa, Y.; Uchimoto, Y.; Ogumi, Z. Direct Observation of Reversible Charge Compensation by Oxygen Ion in Li-Rich Manganese Layered Oxide Positive Electrode Material, $Li_{1.16}Ni_{0.15}Co_{0.19}Mn_{0.50}O_2$. *J. Power Sources* 2015, 276, 89−94.

[12] Gent, W. E.; Lim, K.; Liang, Y.; Li, Q.; Barnes, T.; Ahn, S.-J.; Stone, K. H.; McIntire, M.; Hong, J.; Song, J. H.; et al. Coupling between Oxygen Redox and Cation Migration Explains Unusual

Electrochemistry in Lithium-Rich Layered Oxides. *Nat. Commun.* 2017, 8, 2091.

[13] Assat, G.; Delacourt, C.; Corte, D. A. D.; Tarascon, J.-M. Practical Assessment of Anionic Redox in Li-Rich Layered Oxide Cathodes: A Mixed Blessing for High Energy Li-Ion Batteries. *J. Electrochem. Soc.* 2016, 163, A2965−A2976

[14] Hu, E.; Yu, X.; Lin, R.; Bi, X.; Lu, J.; Bak, S.; Nam, K.-W.; Xin, H. L.; Jaye, C.; Fischer, D. A.; et al. Evolution of Redox Couples in Li- and Mn-Rich Cathode Materials and Mitigation of Voltage Fade by Reducing Oxygen Release. *Nat. Energy* 2018, 3, 690−698

[15] Croy, J. R.; Balasubramanian, M.; Gallagher, K. G.; Burrell, A. K. Review of the U.S. Department of Energy's "Deep Dive" Effort to Understand Voltage Fade in Li- and Mn-Rich Cathodes. *Acc. Chem. Res.* 2015, 48, 2813−2821

[16] Croy, J. R.; Gallagher, K. G.; Balasubramanian, M.; Chen, Z.; Ren, Y.; Kim, D.; Kang, S.-H.; Dees, D. W.; Thackeray, M. M. Examining Hysteresis in Composite x $Li_2MnO_3 \cdot (1-x)LiMO_2$ Cathode Structures. *J. Phys. Chem. C* 2013, 117, 6525−6536

[17] Mortemard de Boisse, B.; Liu, G.; Ma, J.; Nishimura, S.; Chung, S.-C.; Kiuchi, H.; Harada, Y.; Kikkawa, J.; Kobayashi, Y.; Okubo, M.; et al. Intermediate Honeycomb Ordering to Trigger Oxygen Redox Chemistry in Layered Battery Electrode. *Nat. Commun.* 2016, 7, 11397.

[18] Bettge, M.; Li, Y.; Gallagher, K.; Zhu, Y.; Wu, Q.; Lu, W.; Bloom, I.; Abraham, D. P. Voltage Fade of Layered Oxides: Its Measurement and Impact on Energy Density. *J. Electrochem. Soc.* 2013, 160, A2046−A2055

[19] Chen, D.; Kan, W. H.; Chen, G. Understanding Performance Degradation in Cation-Disordered Rock-Salt Oxide Cathodes. *Adv. Energy Mater.* 2019, No. 1901255

[20] Perez, A. J.; Jacquet, Q.; Batuk, D.; Iadecola, A.; Saubanère, M.; Rousse, G.; Larcher, D.; Vezin, H.; Doublet, M.-L.; Tarascon, J.-M. Approaching the Limits of Cationic and Anionic Electrochemical Activity with the Li-Rich Layered Rocksalt Li_3IrO_4. *Nat. Energy* 2017, 2, 954−962.

[21] Foix, D.; Sathiya, M.; McCalla, E.; Tarascon, J.-M.; Gonbeau, D. X-Ray Photoemission Spectroscopy Study of Cationic and Anionic Redox Processes in High-Capacity Li-Ion Battery Layered-Oxide Electrodes. *J. Phys. Chem. C* 2016, 120, 862−874.

[22] Assat, G.; Iadecola, A.; Foix, D.; Dedryvère, R.; Tarascon, J.-M. Direct Quantification of Anionic Redox over Long Cycling of Li-Rich NMC via Hard X-Ray Photoemission Spectroscopy. *ACS Energy Lett.* 2018, 3, 2721−2728

[23] Yang, W.; Devereaux, T. P. Anionic and Cationic Redox and Interfaces in Batteries: Advances from Soft X-Ray Absorption Spectroscopy to Resonant Inelastic Scattering. *J. Power Sources* 2018, 389, 188−197

[24] Tarascon, J.-M.; Gozdz, A. S.; Schmutz, C.; Shokoohi, F.; Warren, P. C. Performance of Bellcore's Plastic Rechargeable Li-Ion Batteries. *Solid State Ionics* 1996, 86−88, 49−54.

[25] Rueff, J.-P.; Ablett, J. M.; Céolin, D.; Prieur, D.; Moreno, T.; Balédent, V.; Lassalle-Kaiser, B.; Rault, J. E.; Simon, M.; Shukla, A. The GALAXIES Beamline at the SOLEIL Synchrotron: Inelastic X-Ray Scattering and Photoelectron Spectroscopy in the Hard X-Ray Range. *J. Synchrotron Radiat.* 2015, 22, 175−179

[26] Rueff, J.-P.; Rault, J. E.; Ablett, J. M.; Utsumi, Y.; Céolin, D. HAXPES for Materials Science at the GALAXIES Beamline. *Synchrotron Radiat. News* 2018, 31, 4−9.

[27] Briois, V.; La Fontaine, C.; Belin, S.; Barthe, L.; Moreno, T.; Pinty, V.; Carcy, A.; Girardot, R.; Fonda, E. ROCK: The New Quick-EXAFS Beamline at SOLEIL. *J. Phys.: Conf. Ser.* 2016, 712,

No. 012149.

[28] Assat, G.; Iadecola, A.; Delacourt, C.; Dedryvère, R.; Tarascon, J.-M. Decoupling Cationic−Anionic Redox Processes in a Model Li-Rich Cathode via Operando X-Ray Absorption Spectroscopy. *Chem. Mater.* 2017, 9714

[29] Lesage, C.; Devers, E.; Legens, C.; Fernandes, G.; Roudenko, O.; Briois, V. High Pressure Cell for Edge Jumping X-Ray Absorption Spectroscopy: Applications to Industrial Liquid Sulfidation of Hydrotreatment Catalysts. *Catal. Today* 2019, 336, 63−73

[30] Leriche, J. B.; Hamelet, S.; Shu, J.; Morcrette, M.; Masquelier, C.; Ouvrard, G.; Zerrouki, M.; Soudan, P.; Belin, S.; Elkaïm, E.; et al. An Electrochemical Cell for Operando Study of Lithium Batteries Using Synchrotron Radiation. *J. Electrochem. Soc.* 2010, 157, A606−A610.

[31] Fauth, F.; Boer, R.; Gil-Ortiz, F.; Popescu, C.; Vallcorba, O.; Peral, I.; Fullà, D.; Benach, J.; Juanhuix, J. The Crystallography Stations at the Alba Synchrotron. *Eur. Phys. J. Plus* 2015, 130, 160

[32] Zhang, R.; Dubouis, N.; Ben Osman, M.; Yin, W.; Sougrati, M. T.; Corte, D. A. D.; Giaume, D.; Grimaud, A. A Dissolution/Precipitation Equilibrium on the Surface of Iridium-Based Perovskites Controls Their Activity as Oxygen Evolution Reaction Catalysts in Acidic Media. *Angew. Chem., Int. Ed.* 2019, 58, 4571−4575

[33] Horsley, J. A. Relationship between the Area of L2,3 X-ray Absorption Edge Resonances and the d Orbital Occupancy in Compounds of Platinum and Iridium. *J. Chem. Phys.* 1982, 76, 1451−1458.

[34] Choy, J.-H.; Kim, D.-K.; Demazeau, G.; Jung, D.-Y. L_{III}-Edge XANES Study on Unusually High Valent Iridium in a Perovskite Lattice. *J. Phys. Chem. A* 1994, 98, 6258−6262.

[35] Lytle, F. W.; Greegor, R. B. Investigation of the '"Join"' between the near Edge and Extended X-ray Absorption Fine Structure. *Appl. Phys. Lett.* 1990, 56, 192−194.

[36] Choy, J.-H.; Kim, D.-K.; Hwang, S.-H.; Demazeau, G.; Jung, D.-Y. XANES and EXAFS Studies on the Ir-O Bond Covalency in Ionic Iridium Perovskites. *J. Am. Chem. Soc.* 1995, 117, 8557−8566.

[37] Laguna-Marco, M. A.; Kayser, P.; Alonso, J. A.; Martínez-Lope, M. J.; van Veenendaal, M.; Choi, Y.; Haskel, D. Electronic Structure, Local Magnetism, and Spin-Orbit Effects of Ir(IV)-, Ir(V)-, and Ir(VI)-Based Compounds. *Phys. Rev. B* 2015, 91, No. 214433.

[38] Tanuma, S.; Powell, C. J.; Penn, D. R. Calculations of Electron Inelastic Mean Free Paths. IX. Data for 41 Elemental Solids over the 50 EV to 30 KeV Range. *Surf. Interface Anal.* 2011, 43, 689−713.

[39] Ben Yahia, M.; Vergnet, J.; Saubanère, M.; Doublet, M.-L. Unified Picture of Anionic Redox in Li/Na-Ion Batteries. *Nat. Mater.* 2019, 18, 496−502.

[40] Perez, A. J.; Batuk, D.; Saubanère, M.; Rousse, G.; Foix, D.; McCalla, E.; Berg, E. J.; Dugas, R.; H. W. van den Bos, K.; Doublet, M.-L.; et al. Strong Oxygen Participation in the Redox Governing the Structural and Electrochemical Properties of Na-Rich Layered Oxide Na_2IrO_3. *Chem. Mater.* 2016, 28, 8278−8288

[41] Dalba, G.; Fornasini, P.; Grisenti, R.; Pasqualini, D.; Diop, D.; Monti, F. Anharmonicity Effects on the Extended X-Ray-Absorption Fine Structure: The Case of Cadmium Selenide. *Phys. Rev. B* 1998, 58, 4793−4802

[42] Kobayashi, H.; Tabuchi, M.; Shikano, M.; Kageyama, H.; Kanno, R. Structure, and Magnetic and Electrochemical Properties of Layered Oxides, Li_2IrO_3. *J. Mater. Chem.* 2003, 13, 957−962